Journal of Magnetic Resonance 298 (2019) 77–84

Contents lists available at ScienceDirect

Journal of Magnetic Resonance

journal homepage: www.elsevier.com/locate/jmr

Variable magnet arrays to passively shim compact permanent-yoke magnets

Till Überrück *, Bernhard Blümich

RWTH Aachen University, Institut für Technische und Makromolekulare Chemie, Worringerweg 2, 52074 Aachen, Germany

ARTICLE INFO

Article history:
Received 27 August 2018
Revised 14 November 2018
Accepted 27 November 2018
Available online 28 November 2018

Keywords:
Passive shimming
Dipole magnets
Bipolar magnets
FEM Simulations/optimization
Pole shoes

ABSTRACT

C-shaped permanent magnets offer a compromise between sample accessability and field strength as well as homogeneity compared to single-sided devices or Halbach arrays. A new approach to passively shim C-shaped dipole magnets is presented. It relies on the magnet poles being constructed from a set of adjustable magnet elements. Two pole concepts are introduced, which allow the correction of the field profile and passively shim the magnet without the need of additional pole shoes or shim pieces.

1. Introduction

Homogenizing the magnetic field has always been the endeavor in Magnetic Resonance (MR) to increase the spectral resolution. Especially the magnetic field of compact permanent magnets lacks homogeneity, due to inhomogeneities of the magnetic material itself and limits in manufacturing precision. Thus, field corrections need to be applied, a process known as shimming. During the last decade great progress has been made [1–3], and compact NMR setups became commercially available that can resolve chemical shift differences in the sub-ppm regime [4,5]. However, these magnets are based on closed designs frequently following the Halbach concept [6], which do not provide open access and set limitation to the sample geometry. On the other hand single-sided sensors like the NMR MOUSE® [7] operate in the stray field of the magnet and are designed to be transported to the sample, e.g. wall paintings or car tires [8–10]. Hence, they do not have any restriction to the sample geometry. Although considerable efforts are made to design single sided magnet arrays with defined magnetic fields [11–13], their stray field remains extremely inhomogeneous, which sets limitations to the Signal to Noise Ratio (SNR) and spectral resolution.

Non-standard applications, e.g. *in-operando* measurements of reactors/batteries or hyperpolarization setups, frequently require additional inserts placed into the magnet or utilize unique sample geometries. Hence, for these kind of experiments a compromise between sample accessibility and field homogeneity is desired. This compromise is provided by dipole magnets that are constructed of two magnet poles facing each other surrounded by a yoke. In the simplest case the yoke is formed like the letter C. Consequently, these magnets are often referred to as C-shaped magnets. However, since the yoke can obtain even more complex and symmetric geometries, we will from here on refer to this type of magnets as yoke magnets. Yoke magnets were prominently used in the early days of magnetic resonance and are still of commercial interest for open MR Imaging (MRI) scanners [14–16].

The basic construction of a yoke magnet obtaining a C-shaped design for demonstrational purpose is outlined in Fig. 1. The magnetic field originates from two disc-shaped permanent magnets that are framed by an iron yoke for flux return and to increase the magnetic field strength between the poles. Since the magnetic field is increasing towards the center of the magnet in the *xy*-direction and decreasing in the *z*-direction, the field profile has a concave or convex shape respectively and pole shoes are added to improve the homogeneity. The pole shoes are made of materials of high magnetic permeability to redirect the magnetic field lines. Their shape design dates back to the work of M.E. Rose in the 1930th [17] and can be simple [15], more sophisticated [18], or even theoretically optimized [19]. Once the field is generally corrected the homogeneity is further increased by either passive and/or active shimming. Whereas passive shimming uses small pieces of magnetic or high permeable material to increase/decrease the field in certain areas [20], active shimming uses shim

* Corresponding author.
E-mail address: Ueberrueck@itmc.rwth-aachen.de (T. Überrück).

https://doi.org/10.1016/j.jmr.2018.11.011
1090-7807/

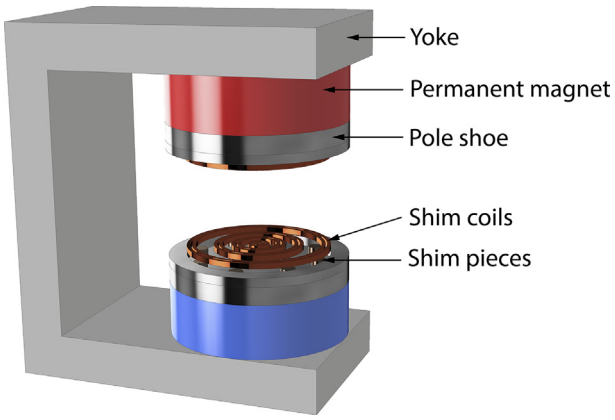

Fig. 1. Basic construction of a conventional C-shaped yoke magnet. The magnet consists of two disc shaped permanent magnets and a yoke for flux return. For passive shimming a pole shoe and additional shim pieces are added. Remaining inhomogeneities are reduced by active shimming using shim coils.

coils to apply field corrections [16,21–24]. Active shims are usually the final step to decrease the inhomogeneity from tens of ppm to the level of ^{1}H chemical shift resolution. Recently, also a passive shim concept for these kinds of sensors was presented, which enabled the ^{1}H chemical shift to be resolved with such magnets [25,26]. Unfortunately, the presented magnet setup does not provide flux return and uses additional pole shoes and shim pieces to correct the magnetic field, which reduces the magnetic field strength down to a ^{1}H resonance frequency of 2.5 MHz and hence limits the range of applications for this shim concept.

Generally, any shim concept that is added on top of the magnets has its drawbacks. Active shims need an external power supply, whereas passive shims employing shim pieces and pole shoes decrease the field strength of the magnet or reduce the accessible gap between the poles significantly [3]. Since the challenge for compact magnets is to minimize the magnet size while maximizing the sample accessibility and usable volume as well as keeping the field strength at an appropriate level, this work addresses new magnet arrays that can substitute the simple disc shaped magnets of the poles and fulfill the purpose of the pole shoe and shim pieces. Our magnet arrays are designed to correct first the curved magnetic profile between the poles and second increase the homogeneity further by displacing individual magnet blocks of the array, while minimizing the loss in sample gap or field strength. Although arrays for yoke magnets have been published [18], they mainly address the optimization of the flux return. To our knowledge no studies on advanced magnet geometries for permanent compact yoke magnets have been reported that are able to correct field inhomogeneities directly.

In the following we present two inexpensive designs for compact yoke magnets. The magnets were optimized using a commercial Finite Element Method (FEM) program in combination with algorithms of the MATLAB® optimization toolbox. A prototype magnet for each array has been constructed, the optimized geometry applied, and residual inhomogeneities were manually corrected. The magnetic fields were visualized with a Gaussmeter mounted on a three-dimensional translation stage. Simple NMR experiments were performed to demonstrate the achieved field homogeneity.

2. Pole design

The concept of the magnet arrays is to create a closed magnetic surface from individual magnet blocks that are displaceable in height to correct the curved field profile originating from the flat poles and hence shim the magnet. By substituting solid magnet discs by an array of smaller elements imperfections of the single magnets become less crucial and can be additionally accounted for by individual displacements of the elements.

Inspired by the field of tessellation of 2D planes, there are only three simple and symmetric polygons that can be used to fill a plane continuously – triangles, squares, and hexagons. The first pole design is based on hexagons due to their higher rotational symmetry compared to the other two polygons and the higher mechanical stability of the magnetic material caused by the shallower angle of the edges. The actual design resulted in a basic honeycomb pattern, meaning that three shells of hexagonal magnets are arranged around one hexagonal center piece, resulting in a total number of 37 magnet blocks per pole (Fig. 2a).

As a number of 37 adjustable blocks per pole results in a total of 73 variables to shim the magnet (one hexagonal block is considered as a reference point), the second design reduces the number of variables by substituting the three shells made of hexagons by simple magnet rings (Fig. 2b). This leads to higher symmetry and reduces the number of variables to six or as the two inner rings can be slightly tilted in the *xy*-plane to eighteen. However, by substituting the individual blocks with solid rings the inhomogeneity of the magnetic material becomes a major issue again. One idea to reduce the inherent inhomogeneity of magnet rings was presented by Utsuzawa et al. They stacked layers of ring magnets onto each other and rotated them in a numerically optimized way so that the inhomogeneities of the individual rings cancel each other [13]. For our pole design four layers of magnet rings were stacked. Additionally, the thickness of the inner ring stacks and the cylindrical center magnet was decreased to reduce the curvature of the field profile right from the start. The magnet pieces used for the simulation and construction of both yoke magnets are listed in Table 1.

3. Simulation

Before constructing a prototype for each magnet, the magnetic fields and magnet displacements were simulated and theoretically optimized to generally correct the curved profile originating from flat magnet poles. All simulations were conducted with the commercial FEM program COMSOL Multiphysics® 5.2. The Optimization of the magnet displacements utilized the patternsearch algorithm of the MATLAB® R2015a optimization toolbox. This algorithm is a simple displacement algorithm that increases and decreases each optimization variable iteratively by a certain distance and calculates the corresponding value of the target function. If one of the calculated target values is better than the one of the

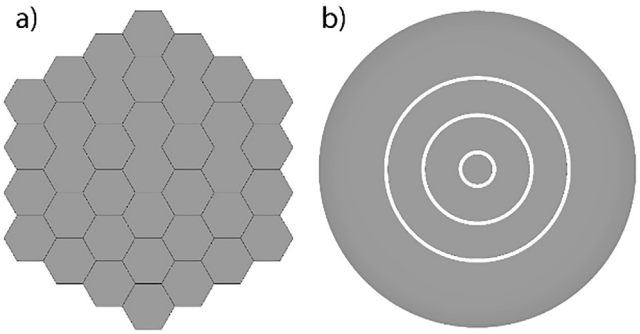

Fig. 2. Design of the magnet arrays. (a) Magnet pole consisting of 37 hexagonal magnet blocks with a maximum diameter of 36.4 mm. (b) Magnet pole with a total diameter of 42.0 mm consisting of three shells of ring magnets around a center magnet cylinder.

Table 1
$Nd_2Fe_{14}B$ magnet elements used for the simulation and construction of both magnets.

	Quantity	d_{out} [mm]	d_{in} [mm]	h [mm]	Material	Remanence [T]
Hexagonal	74	5.2	–	15	N52	1.43–1.48
Ring	4	42	25	3	N35	1.17–1.22
	4	24	15	2	N35	1.17–1.22
	4	14	5	2	N35	1.17–1.22
	6	4	–	1	N38	1.22–1.25

previous iteration, the new displacements are accepted and the displacement distance is halved. If not, the new displacements are rejected and the displacement distance is doubled. Although there is no guarantee that this algorithm finds the absolute minimum/maximum of the target function, it resembles the actual shimming process of the magnet and delivered robust results in our simulations.

The FEM program uses CAD models to calculate the magnetic flux density between the poles (Fig. 3a/c). The hexagonal magnet arrays (a) are mounted on a double-sided yoke as the individual magnet blocks allow an asymmetric adjustment of the magnetic field, whereas the yoke of the ring magnet (c) has 4 columns to assure a more symmetric flux return. The blue spheres between the poles symbolize the Volume Of Interest (VOI), in which the magnetic field is optimized. This region is evaluated on a much finer mesh than the remaining parts of the magnet. The diameter of the pole is approximately 30–36 mm for the hexagonal magnet and the gap between the poles is 17 mm without any magnet displacements applied. The ring magnet has a pole diameter of 42 mm and 20 mm gap.

The calculation of the magnetic field without any magnet displacements results in the expected curved profile for both magnets (Fig. 4 – blue curves). The magnetic field of the hexagonal magnet is higher than the ring magnet due to the smaller pole gap. Also, the curved field profile of the ring magnet is distorted, especially in z-direction, due to the reduced height of the inner rings (Fig. 3b). However, the optimization process of the magnet displacements to gain a more homogeneous profile needs some further simplifications as particularly the 37 variables of the hexagonal magnet would increase the computing time significantly. Considering the distances of the individual magnets from the center it is seen that the number of variables for the hexagonal magnet can be reduced to 5 (Fig. 3a). The magnets in the first shell (red) have all the same distance, whereas in the second (blue) and third (yellow) shell there are only two different distances of the magnets. Of course, this reduction of variables neglects effects resulting from the asymmetry of the yoke and from magnet imperfections, but it is reasonable on account of the savings in computing time and sufficient to gain a general correction of the magnetic field profile. The number of variables of the ring magnet does not need any simplifications. As there are only two inner rings plus the center column shaped magnet that can be displaced relative to the outer ring, the optimization uses three variables.

The geometry of both magnets is optimized in two steps. First the inhomogeneity I of the magnetic field B_0

$$I = \frac{\max(B_0) - \min(B_0)}{\mathrm{mean}(B_0)} \tag{1}$$

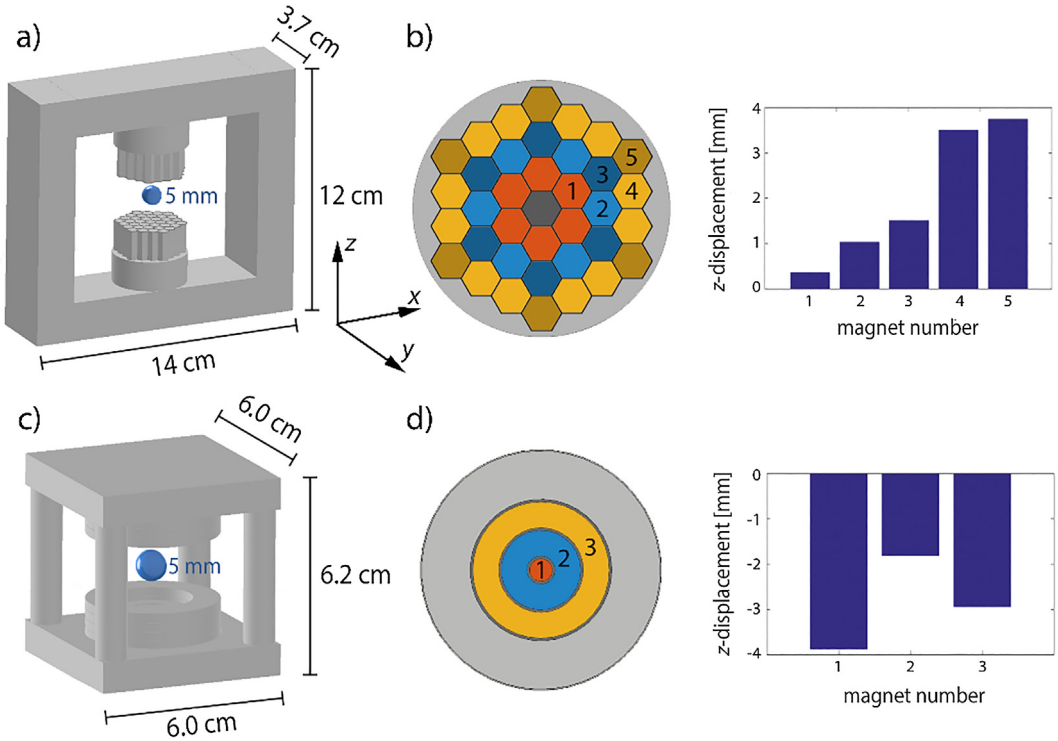

Fig. 3. FEM simulations. (a) CAD model of the hexagonal magnet with the Volume of Interest (VOI) in the center (blue). The number of optimization variables is reduced to five due to symmetry considerations. (b) Optimized displacement of the hexagonal magnet blocks in a spherical VOI of 5 mm diameter. (c) CAD model of the ring magnet with the VOI in the center (blue). The number of optimization variables is three. (d) Optimized displacement of the magnet rings in a spherical VOI of 5 mm diameter. (For interpretation of the references to colour in this figure legend, the reader is referred to the web version of this article.)

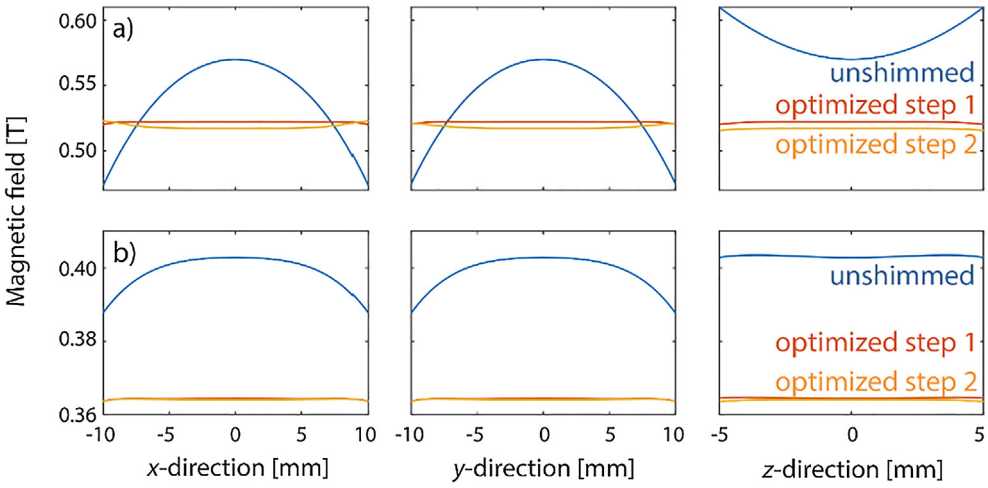

Fig. 4. Simulated magnetic field profiles before and after shimming. (a) Cross sections of the magnetic field profile of the hexagonal magnet along the three-spatial dimensions. The profile without any magnet displacements (blue) is compared to the optimized one in an elliptic VOI of maximum diameters $20 \times 20 \times 10$ mm^3 (red) and to one optimized in a spherical VOI of 5 mm diameter (yellow). (b) Cross sections of the magnetic field profile of the ring magnet. The profile without any magnet displacements (blue) is compared to the optimized one in an elliptic VOI of maximum diameters $20 \times 20 \times 10$ mm^3 (red) and to one optimized in a spherical VOI of 5 mm diameter (yellow). Additional zoom in figures are presented in the eSI. (For interpretation of the references to colour in this figure legend, the reader is referred to the web version of this article.)

is decreased in a large elliptic VOI of maximum *x*- and *y*-diameters of 20 mm and a *z*-diameter of 10 mm to correct the field profile throughout the whole magnet gap. For the starting positions all variables are set to zero and the finishing criterion of the optimization process was set to a displacement of 0.1 μm. The optimization of the hexagonal magnet took 110 iterations and the one of the ring magnet 94. Secondly, the VOI is scaled down to a sphere of 5 mm diameter, which resembles the actual size of a standard NMR sample tube and the optimization is restarted using the optimized displacements from the first optimization step as starting positions. The optimization process stopped after 30 for the hexagonal magnet and 22 iterations for the ring magnet.

The optimized displacements of the hexagonal magnet result in a convex shape (Fig. 3b) and correct the concave profile of the field in *xy*- and convex profile in the *z*-direction (Fig. 4a). Whereas the field is generally corrected after the first iteration step (red) by redistributing the magnetic flux density in the magnet gap and yields in an increase of chemical shift resolution by about two orders of magnitude (Table 2), the second step (yellow) further raises the magnetic field in the outer *xy*-area of the magnet. This raise reduces a residual parabolic curvature in the center region of the *xy*-direction and additionally flattens the center profile in *z*-direction (eSI, Fig. 5). Consequently, the chemical shift resolution is improved by half an order of magnitude in the spherical VOI of 5 mm diameter (Table 2). Our results are qualitatively similar to those obtained by the optimization of the pole shoe geometry [19]. The only difference is that the pole shoes optimized by Ryu et al. have a small bump in the middle suggesting that the center magnet in our simulations would need to be displaced. This center magnet block was used as a reference point so far. However, using the second shell as reference and the center magnet as the first optimization variable does not improve the homogeneity in our simulations. We suggest that the bump in the pole shoe optimization is caused by the reduction of the magnetic material. Reducing the magnetic material of a pole shoe is a slightly different approach than the displacement of magnet blocks with a fixed amount of magnetic material throughout the whole optimization process.

The optimized displacements of the ring magnet (Fig. 3d) do not follow a convex path. Although the inner magnets are lowered with respect to the outer ring (It is noted that the surface of the outer ring is at the 0 mm mark and the magnets are lowered to this reference as indicated by the minus sign (Fig. 3c/d)), the second shell ring magnet is pushed down less than the third shell magnet and the cylindrical center magnet. Hence, this optimized shape obtains a bump in the center region comparable to [19] and is in line with our hypothesis of the influence of the magnetic material on the optimization results, since the thickness of the inner rings and the center magnet is smaller than that of the outer ring.

The optimized displacements correct the magnetic profile significantly (Fig. 4b) and increase the homogeneity of the magnet by one to two orders of magnitude resulting in a chemical shift resolution of 33 ppm in a spherical VOI of 5 mm diameter. Whereas the first iteration run corrects the general shape, the second run increases the magnetic field density at the outer part of the magnet array, which again flattens a parabolic curvature in the center region of the *xy*-dimension and a negative curvature in the *z*-direction (eSI, Fig. 5). Although the achieved chemical shift resolution is slightly more homogeneous than the one for the hexagonal magnet array especially considering the larger gap, one has to keep in mind that for the hexagonal array the influence of the asymmetric yoke was neglected and that the ring magnet has a more symmetric yoke and a larger pole diameter.

Table 2
Comparison of the chemical shift resolution before and after the first and second steps of the FEM optimization in an elliptic VOI (max. diameters $20 \times 20 \times 10$ mm^3) and a spherical one of 5 mm diameter.

	VOI [mm^3]	START [ppm]	STEP 1 [ppm]	STEP 2 [ppm]
Hexagonal	$20 \times 20 \times 10$	232 000	4 800	17 600
	$5 \times 5 \times 5$	26 000	160	36
Ring	$20 \times 20 \times 10$	44 0	4 000	4 300
	$5 \times 5 \times 5$	2 000	40	33

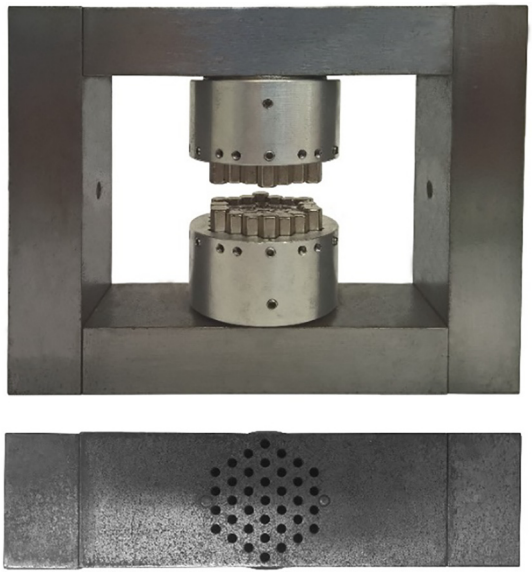

Fig. 5. Side and top views of the hexagonal magnet. At the top and bottom of the yoke are 37 holes to displace the hexagonal magnet blocks in height.

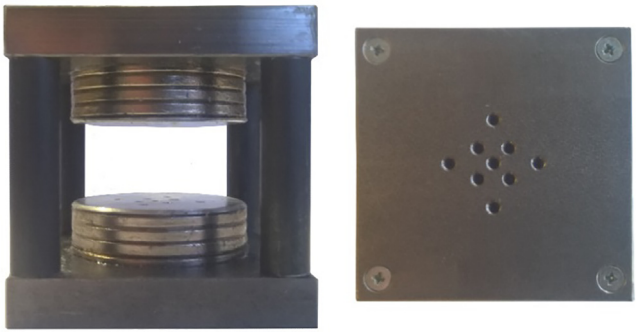

Fig. 6. Side and top views of the ring magnet. At the top and bottom of the yoke are nine holes to slightly tilt the inner magnet ring stacks and to move the center magnet in height.

4. Construction

Both prototypes (Figs. 5 and 6) were built following the design presented in the simulation section. The $Nd_2Fe_{14}B$ magnets listed in Table 1 were ordered from commercial suppliers (hexagonal: BR Technik Kontor GmbH, ring: HKCM® Engineering e.K.). The costs of the magnetic material used to construct each prototype were less than 100 €. The yokes were manufactured from pure iron by the inhouse mechanical workshop. The hexagonal magnet blocks were characterized with a Lakeshore 420 Gaussmeter and afterwards assembled. Since the individual magnet blocks repel each other, they were hold in place during the construction process by zip ties and aluminum support rings, which could fix the individual shells of magnets. For further details the reader is referred to the electronic SI of the paper. The assembled poles were mounted on the yoke and fixed by larger aluminum supports with M3 Allen bolts at the side to hold the magnet blocks in place. At the top and bottom of the yoke 37 small holes were drilled so that the magnet blocks can be displaced in height using M3 Allen bolts. The weight of the final magnet is about 2.8 kg, mainly caused by the heavy yoke.

The poles of the ring magnet (Fig. 2) consist of three rings of magnetic material and one center column magnet. Each ring was constructed as a stack of four layers of ring magnets. The stacks of ring magnets were homogenized following the procedure described in [13]. A more detailed discussion of the homogenization procedure is presented in the electronic SI. The homogenized magnet stacks are glued together and mounted on the yoke. The center column magnet is constructed from a stack of six one-millimeter thick disc shaped magnets. The residual volume inside the poles is filled with elastic spacer material and the top of the pole sealed with an aluminum plate. At the bottom and top of the yoke are nine holes to access M3 Allen bolts and displace and tilt the two inner magnet stacks and the center magnet cylinder. The final weight of the magnet is 0.85 kg.

5. Shimming and characterization

The assembled magnets were shimmed and characterized using a Lakeshore® 420 (accuracy 1 G) or F.W. Bell® 7010 Gaussmeter (accuracy 0.1 G), which were mounted on a three-dimensional translation stage (ISEL® LES4). The stage and Gaussmeter are controlled by an inhouse MATLAB routine.

Without any displacement of magnet elements, the magnets have strongly inhomogeneous magnetic fields (eSI, Fig. 3a/c). However, after applying the optimized magnet displacements the field profiles are clearly improved. The magnet with hexagonal poles shows a generally corrected region of about 20 mm diameter and the actual hexagonal shape of the magnet pole becomes visible (eSI, Fig. 3b). For the magnet with ring poles the flattened field area obtains a round shape of approximately 20 mm diameter too (eSi, Fig. 3d).

Still residual field inhomogeneities in the range above thousand ppm in a spherical center region of 5 mm in diameter were present due to manufacturing imperfections and polarizations of the hexagonal magnet elements. These inhomogeneities were minimized in an initial attempt by utilizing Gaussmeter field maps and increasing or decreasing the magnetic field at necessary positions by adjusting the height of individual blocks or the tilt of the ring magnet stacks. This shimming process was done iteratively by measuring the field at three different height and another profile in z-direction. If the center profile obtained deviations from the mean magnetic field in the center, the magnet block at the corresponding position was adjusted under additional considerations of the other two maps acquired at a lower and higher level. Whereas this process took several iterations for the hexagonal magnet in a timeframe of a few weeks, caused by the number of variables, the shimming of the ring magnet needed many fewer iterations and was done in a few days. Comparing the profiles shimmed in this first shimming approach with the simulated data (Fig. 7), it is seen that the overall curve shapes agree well. The field strengths of both magnets is slightly lower than the ones predicted by theory, which could be caused by an insufficient flux return, minor deviations in the gap height, or by temperature effects. However, when the actual center region is evaluated on a finer scale (eSI, Fig. 6), it is seen that the profiles gained from simple Hall-probe shimming are still inhomogeneous in the order of 100–300 ppm in a spherical center region of 5 mm in diameter.

6. Relaxation and spectroscopy

As the available Hall probes are limited to maximum resolutions in the order of 10^{-5} T and the homogeneity that was achieved by shimming with a setup relying on these devices did not exceed ranges beyond 100 ppm, we set out to determine and increase the homogeneity further by simple ^{1}H NMR experiments. For this purpose, a probe with a solenoid coil of approximately 4 mm diameter

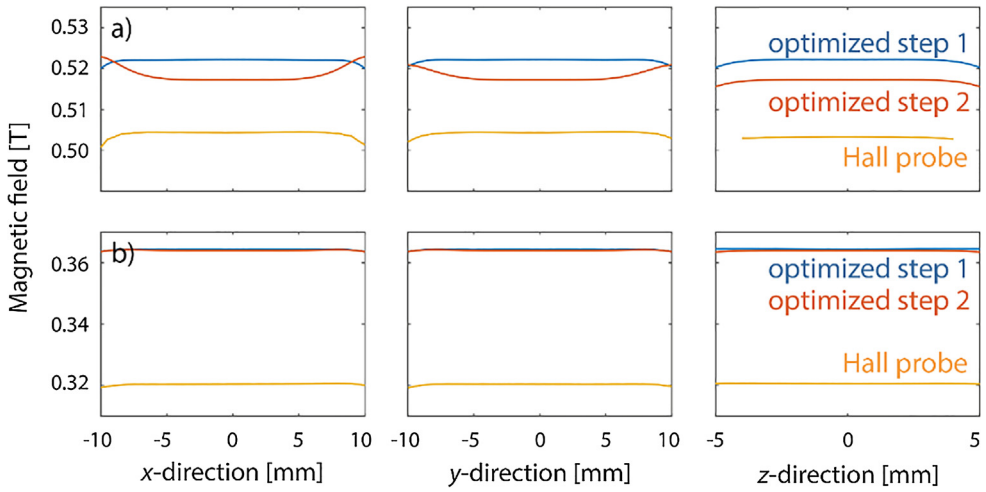

Fig. 7. Comparison of the measured magnetic field profiles (resolution 0.5 mm) and the simulated data. (a) Cross sections of the magnetic field profile of the magnet with hexagonal poles along the three-spatial dimensions. The measured profile (yellow) is compared to the two theoretical profiles of the optimization (blue and red). (b) Cross sections of the magnetic field profile of the magnet with ring poles. The measured profile (yellow) is compared to the two theoretical profiles of the optimization (blue and red). Additional zoom in figures are presented in the eSI. (For interpretation of the references to colour in this figure legend, the reader is referred to the web version of this article.)

and 4 mm in length was built and connected to a Magritek® KEA^2 spectrometer running with PROSPA V3.22. The sample was deionized water in a 4 mm standard NMR tube. The ^{1}H resonance frequency was 21.4 MHz for the hexagonal magnet and 13.7 MHz for the ring magnet. While acquiring ^{1}H spectra, small adjustments of the magnet elements were made in an iterative way to increase the decay time of the FIDs and consequently improve the homogeneity of the magnets further.

After the decay times were increased in the best possible manner, CPMG experiments reported T_2 times of around 1.6 s for both magnets (Table 3). The decay curves were acquired with 2048 echoes and echo times of 3–5 ms. Only two scans were needed to result in a residual R^2 for the mono-exponential curve fits greater than 0.999. The accuracy of the fits and the magnitudes of T_2, demonstrate the increase in homogeneity and the usability of both magnets for relaxation NMR studies with a good SNR compared to single sided sensors, where the T_2 of water does not exceed the hundreds of milliseconds range. The results of our magnets are despite of their small size qualitatively at the same level as the ones gained with commercial relaxometry devices like the Bruker® Minispec, which resulted in T_2 values of 1.8–2 s for the same sample and similar acquisition settings.

Further, the homogeneity is characterized by simple ^{1}H NMR spectra, which were acquired with 16 scans (Fig. 8) and yielded in a SNR greater than 200. The SNR was calculated as the ratio of the signal amplitude to the standard deviation of the noise at the edges of the spectra. The chemical shift resolution was determined at the Full Width at Half Maximum (FWHM) and resulted in 16 ppm for the hexagonal and 29 ppm for the ring magnet. These values are in the range of the predicted ones gained from the simulation (Table 3). For the magnet with hexagonal poles the chemical shift resolution is slightly higher than in the simulation, which

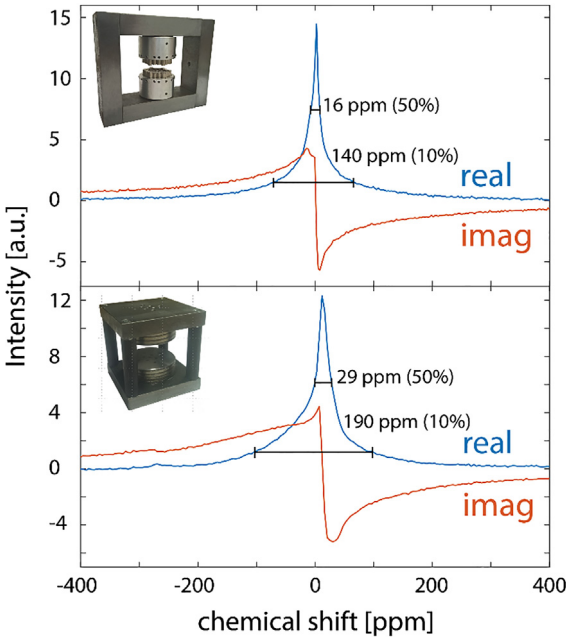

Fig. 8. NMR spectra of a 4 mm diameter deionized water sample. (a) The spectrum (22.4 MHz) acquired with the hexagonal magnet yields a chemical shift resolution (FWHM) of ∼16 ppm. (b) The spectrum (13.7 MHz) acquired with the ring magnet yields a resolution of ∼29 ppm.

is probably caused by the manual corrections due to the asymmetry of the yoke that the simulation did not account for. The homogeneity of the ring magnet is slightly worse than that predicted by

Table 3
Comparison of the chemical shift resolution of the simulated and the measured data. Additionally, the T_2 relaxation times for both magnets are listed.

	Simulation (4 mm)	Spectrum at 50% (4 mm)	Spectrum at 10% (4 mm)	Spectrum at 1% (4 mm)	T_2 (4 mm)
Hexagonal	26 ppm	16 ppm	140 ppm	670 ppm	1.6 s
Ring	27 ppm	29 ppm	190 ppm	550 ppm	1.6 s

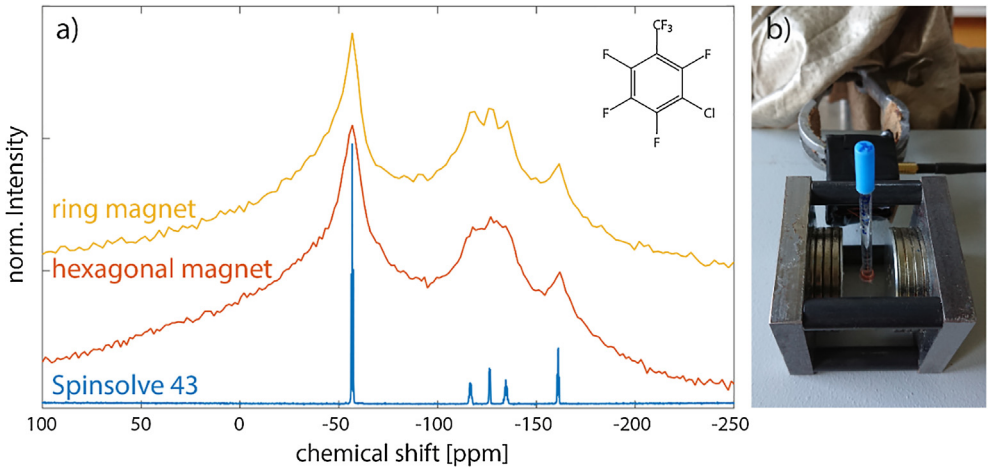

Fig. 9. ^{19}F NMR measurements of 3-Chloro-2,4,5,6-tetrafluorobenzotrifluoride. (a) Comparison of ^{19}F spectra acquired with the ring magnet (12.8 MHz), the hexagonal magnet (20 MHz), and a Magritek® Spinsolve 43 (40.7 MHz). The basic molecular structure that is resolved by a closed geometry benchtop spectrometer is identified with both open-access magnets. (b) Simple experimental setup that the spectra were acquired with. The magnet is not shielded or temperature controlled and the gap is completely accessible.

the simulation. This deviation is most likely due to residual inhomogeneities of the magnet ring stacks that have not been eliminated by the prior homogenization procedure (construction section and eSI).

To further demonstrate the homogeneity of both magnets additional ^{19}F spectra of 3-Chloro-2,4,5,6-tetrafluorobenzotrifluoride were acquired using the same coil geometry and experimental setup as before (Fig. 9). The displacements for individual magnets had to be slightly adjusted again for both prototypes as temperature changes and further tests had altered the previous ones. The number of scans has been set to 32 for both spectra. A comparison to a spectrum acquired in a standard benchtop spectrometer (40 scans) with a closed geometry shows that both open access magnet designs can resolve the basic features of the molecular spectrum. Even the ^{19}F nuclei of the benzene ring that are visible at higher frequencies are distinguishable and hence the spectra confirm the ppm resolution range that was predicted in the FWHM of the ^{1}H spectra.

7. Conclusion

In this study two new magnet geometries for compact dipole yoke magnets have been introduced. The magnets are designed to correct the field profile by displacing individual magnet elements comparable to shimming concepts frequently applied to Halbach magnets [1]. This approach eliminates the need for additional pole shoes and shim pieces and preserves the original field strength of the magnets or the accessible sample gap between the poles. Both magnet geometries were optimized using FEM methods, and inexpensive prototypes were constructed. The increase in homogeneity is about two to three orders of magnitude yielding spectral resolutions with which simple ^{19}F spectra could be resolved. A direct comparison of the magnet with hexagonal blocks and the one with ring magnets shows that with the hexagonal tessellation pattern slightly better homogeneity can be achieved than with a geometry that is even more symmetric. This means even if the original magnetic material is imperfect, tessellation patterns can reduce and compensate these imperfections, whereas bigger magnet blocks will always remain difficult to homogenize. Hence in the future the tessellation approach could be continued and further extended to more advanced geometric patterns like the Penrose patterns that can better approximate a circular pole geometry.

Acknowledgment

The authors are grateful for the support by the Deutsche Forschungsgemeinschaft (DFG – Project: BL231/49-1). Additional thank is expressed to Klaus Kupferschläger, who did the basic design of the yoke of the hexagonal magnet.

Appendix A. Supplementary material

Supplementary data associated with this article can be found, in the online version, at https://doi.org/10.1016/j.jmr.2018.11.011.

References

[1] E. Danieli, J. Perlo, B. Blümich, F. Casanova, Small magnets for portable NMR spectrometers, Angew. Chem. - Int. Ed. 49 (2010) 4133–4135, https://doi.org/10.1002/anie.201000221.
[2] A.J. Parker, W. Zia, C.W.G. Rehorn, B. Blümich, Shimming Halbach magnets utilizing genetic algorithms to profit from material imperfections, J. Magn. Reson. 265 (2016) 83–89, https://doi.org/10.1016/j.jmr.2016.01.014.
[3] A. McDowell, E. Fukushima, Ultracompact NMR:1H spectroscopy in a subkilogram magnet, Appl. Magn. Reson. 35 (2008) 185–195, https://doi.org/10.1007/s00723-008-0151-3.
[4] B. Blümich, K. Singh, Desktop NMR and its applications from materials science to organic Chemistry, Angew. Chemie Int. Ed. (2017) 2–17, https://doi.org/10.1002/anie.201707084.
[5] B. Blümich, Introduction to compact NMR: a review of methods, TrAC Trends Anal. Chem. 83 (2016) 2–11, https://doi.org/10.1016/j.trac.2015.12.012.
[6] K. Halbach, Design of permanent multipole magnets with oriented rare earth cobalt material, Nucl. Instrum. Meth. 169 (1980) 1–10, https://doi.org/10.1016/0029-554X(80)90094-4.
[7] B. Blümich, P. Blümler, G. Eidmann, A. Guthausen, R. Haken, U. Schmitz, K. Saito, G. Zimmer, The NMR-mouse: construction, excitation, and applications, Magn. Reson. Imag. 16 (1998) 479–484, https://doi.org/10.1016/S0730-725X(98)00069-1.
[8] B. Blümich, F. Casanova, J. Perlo, F. Presciutti, C. Anselmi, B. Doherty, Noninvasive testing of art and cultural heritage by mobile NMR, Acc. Chem. Res. 43 (2010) 761–770, https://doi.org/10.1021/ar900277h.
[9] B. Blümich, J. Perlo, F. Casanova, Mobile single-sided NMR, Prog. Nucl. Magn. Reson. Spectrosc. 52 (2008) 197–269, https://doi.org/10.1016/j.pnmrs.2007.10.002.
[10] F. Casanova, J. Perlo, B. Blümich, Single Sided NMR, Springer, Berlin, Heidelberg, 2011. http://doi.org/10.1007/978-3-642-16307-4_5.
[11] J. Perlo, F. Casanova, B. Blümich, Single-sided sensor for high-resolution NMR spectroscopy, J. Magn. Reson. 180 (2006) 274–279, https://doi.org/10.1016/j.jmr.2006.03.004.
[12] K.S. Panesar, C. Hugon, G. Aubert, P. Judeinstein, J.-M. Zanotti, D. Sakellariou, Measurement of self-diffusion in thin samples using a novel one-sided NMR magnet, Microporous Mesoporous Mater. 178 (2013) 79–83, https://doi.org/10.1016/j.micromeso.2013.04.016.
[13] S. Utsuzawa, E. Fukushima, Unilateral NMR with a barrel magnet, J. Magn. Reson. 282 (2017) 104–113, https://doi.org/10.1016/j.jmr.2017.07.006.

[14] R.S. Sahebjavaher, K. Walus, B. Stoeber, Permanent magnet desktop magnetic resonance imaging system with microfabricated multiturn gradient coils for microflow imaging in capillary tubes, Rev. Sci. Instrum. 81 (2010), https://doi.org/10.1063/1.3280171.
[15] Wu. Chunli, Jialiang Guo, Chuan Chen, Guo Yan, Chengshan Li, Optimal design and test of main magnet in superconducting MRI, IEEE Trans. Appl. Supercond. 20 (2010) 1810–1813, https://doi.org/10.1109/TASC.2010.2041648.
[16] Y. Terada, S. Kono, K. Ishizawa, S. Inamura, T. Uchiumi, D. Tamada, K. Kose, Magnetic field shimming of a permanent magnet using a combination of pieces of permanent magnets and a single-channel shim coil for skeletal age assessment of children, J. Magn. Reson. 230 (2013) 125–133, https://doi.org/10.1016/j.jmr.2013.02.005.
[17] M.E. Rose, Magnetic field corrections in the cyclotron, Phys. Rev. 53 (1938) 715–719.
[18] A. Podol'skii, Development of permanent magnet assembly for MRI devices, IEEE Trans. Magn. 34 (1998) 248–252, https://doi.org/10.1109/20.650251.
[19] J.S. Ryu, Y. Yao, C.S. Koh, Y.J. Shin, 3-D optimal shape design of pole piece in permanent magnet MRI using parameterized nonlinear design sensitivity analysis, IEEE Trans. Magn. 42 (2006) 1351–1354, https://doi.org/10.1109/TMAG.2006.871563.
[20] Z. He, W. He, J. Guo, An optimized passive shimming method for Bi-planar permanent MRI Magnets, Appl. Magn. Reson. 48 (2017) 871–887, https://doi.org/10.1007/s00723-017-0908-7.
[21] Y. Terada, D. Tamada, K. Kose, Development of a temperature-variable magnetic resonance imaging system using a 1.0 T yokeless permanent magnet, J. Magn. Reson. 212 (2011) 355–361, https://doi.org/10.1016/j.jmr.2011.07.016.
[22] A. McDowell, M. Conradi, Thin high-order shims for small dipole NMR magnets, J. Magn. Reson. 281 (2017) 7–16, https://doi.org/10.1016/j.jmr.2017.04.013.
[23] D. Tamada, K. Kose, T. Haishi, A new planar single-channel shim coil using multiple circular currents for magnetic resonance imaging, Appl. Phys. Exp. 5 (2012), https://doi.org/10.1143/APEX.5.056701.
[24] S. Chen, T. Xia, Z. Miao, L. Xu, H. Wang, S. Dai, Active shimming method for a 21.3 MHz small-animal MRI magnet, Meas. Sci. Technol. 28 (2017), https://doi.org/10.1088/1361-6501/aa61b1.
[25] K. Chonlathep, T. Sakamoto, K. Sugahara, Y. Kondo, A simple and low-cost permanent magnet system for NMR, J. Magn. Reson. 275 (2017) 114–119, https://doi.org/10.1016/j.jmr.2016.12.010.
[26] Y. Hibino, K. Sugahara, Y. Muro, H. Tanaka, T. Sato, Y. Kondo, Simple and low-cost tabletop NMR system for chemical-shift-resolution spectra measurements, J. Magn. Reson. 294 (2018) 128–132, https://doi.org/10.1016/j.jmr.2018.07.003.